Experiments in the Hydrodynamic Modeling of an Underwater Manipulator

Timothy W. McLain
Department of Mechanical Engineering
Brigham Young University
Provo, UT 84602

Stephen M. Rock
Department of Aeronautics and Astronautics
Stanford University
Stanford, CA 94305

Abstract — **In this paper, the hydrodynamic modeling of a cylindrical single-link manipulator undergoing typical robotic slews is investigated. The basis of the model presented here is a two-dimensional potential-flow theory analysis of a cylinder undergoing unsteady motions. This analysis was extended semi-empirically to three dimensions using strip theory. The analysis demonstrated that drag and added-mass coefficients for a single-link arm swinging from one position to another are not constant, but are dependent on how far the cylinder has rotated.**

Experiments were conducted both to characterize the state-dependent behavior of the hydrodynamic coefficients and to validate the hydrodynamic model for a variety of motions. For these experiments, a circular cylinder (length/diameter = 9.1) was swung about its end through moderate angles (< 120 degrees) in a start-stop fashion common to manipulation tasks. By using coefficients identified under the assumption of state-dependent behavior in the single-link arm model, a significant improvement in modeling accuracy over results from standard constant-coefficient models was achieved.

1 Introduction

The goal of the research presented in this paper was to develop an understanding of the hydrodynamic forces acting on an underwater manipulator as it moves through the water, and based on that understanding, to develop an accurate predictive model of the hydrodynamic forces.

As a first step towards achieving this goal, an experimental investigation of the hydrodynamic forces acting on a swinging single-link arm was undertaken. A single-link, single-degree-of-freedom arm was chosen for two main reasons: First, it represents a challenging, yet manageable problem that can be studied at a fundamental level. Second, it shares many of the unique hydrodynamic attributes of a multiple-link, multiple-degree-of-freedom arm (*e.g.,* short, accelerative, highly-rotational motions, end effects, etc.).

Accurate hydrodynamic models have potential for use in a number of applications. High-quality station-keeping performance of an underwater arm/vehicle system using a model-based decoupling controller has been demonstrated experimentally [1]. Other potential control applications include manipulator feedback control design, where interlink coupling may be significant, or optimal trajectory planning where minimum-time or minimum energy trajectories could be determined based on hydrodynamic model information.

Other applications for models include real-time simulation of underwater robotic systems for pilot training purposes and underwater manipulator design, where an estimate of dynamic torque requirements would allow motors, reducers, and sensors to be designed and selected with greater certainty.

For applications involving real-time simulation or control, it is necessary that the hydrodynamic models be implementable in real time, sometimes with limited computing resources. For these applications, state-of-the-art methods from the field of computational fluid dynamics are not applicable.

The recent papers of Lévesque and Richard [2], McMillan *et al.* [3], and Tarn *et al.* [4] have each addressed the modeling of underwater robotic systems. The focus of these papers was on the incorporation of hydrodynamic effects into the equations of motion describing the dynamic behavior of underwater robotic systems and on efficient computational methods for solving these equations. The models presented were each strip-theory-based and recommended using standard constant values for the drag and added-mass coefficients. None of those models was validated experimentally.

The experimental results presented here show that the conditions under which the use of standard coefficients is valid are violated for typical robotic motions due to spanwise flow and end effects. In the model developed here, these three-dimensional-flow effects are accounted for explicitly in the state-dependent hydrodynamic coefficients identified from experiments.

2 Experimental Apparatus

Figure 1 shows schematically the apparatus used for the experiments of this paper. The single-link, single-degree-

of-freedom arm used here consisted of a 7.1 cm diameter, 65 cm long hollow PVC cylinder driven by a variable reluctance motor with a harmonic-drive reducer. The arm was mounted so that it rotated about one end in the horizontal plane in a swinging motion. A cylinder of circular cross-section was chosen because of its axisymmetric shape, which makes it well-suited for an underwater manipulator: Its shape is easily fabricated, it accommodates actuator components (motors, reducers) well, and hydrodynamic forces are independent of the orientation of its cross section with respect to the flow.

To aid in the characterization of the hydrodynamic forces, several different types of sensors were used. The arm joint angle was measured using a capacitative encoder mounted on the motor shaft. An estimate of the arm angular velocity was obtained by taking the first difference of the position signal and then filtering it digitally with a fourth-order Butterworth low-pass filter with a 50 Hz cut-off frequency. The angular acceleration of the arm joint was sensed using a linear solid-state accelerometer mounted in the arm at a known distance from the arm hub. Measurements of output-shaft torque (T) and lift moment (M_{lift}) at the arm hub were made available through a specially-designed, strain-gage-instrumented beam element connecting the output shaft to the base of the arm.

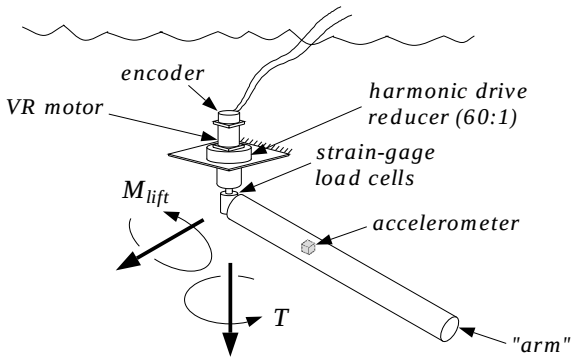

Figure 1: Single-Link Arm, Actuator, and Sensors

3 Modeling Approach

3.1 Theoretical Analysis

To arrive at a model form, upon which a full three-dimensional model of the hydrodynamic forces on a rotating cylinder could be built, a two-dimensional potential-flow analysis of a circular cylinder undergoing unsteady motions was developed from first principles. This 2-D analysis was later extended to three dimensions using strip theory.

Two-Dimensional Analysis The 2-D analysis considers the flow of a nominally incompressible, inviscid fluid over a cylinder that is moving through the fluid with unsteady motions. The wake and feeding layers are modeled using discrete vortices with independent positions, velocities, and strengths. Figure 2 shows a schematic representation of the 2-D cylinder and its wake. The 2-D portion of this analysis is similar in approach to that done by Sarpkaya [5, 6] for a stationary cylinder immersed in a moving fluid.

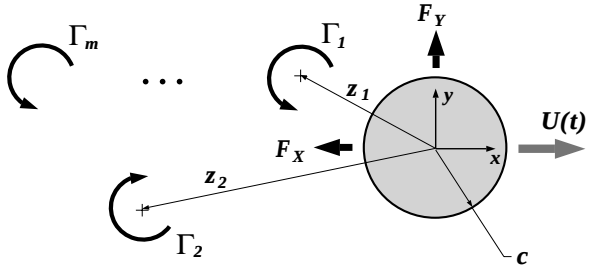

Figure 2: Two-Dimensional Hydrodynamic Model

Using Blasius' theorem [7], the forces acting on a moving circular cylinder in a still fluid in the presence of a specified number of singularities can be calculated by

$$F_X - iF_Y = i\frac{\rho}{2}\int_C \left(\frac{dw}{dz}\right)^2 dz - i\rho\frac{\partial}{\partial t}\int_C \overline{w}\, d\bar{z} + \rho A\frac{d\overline{W}}{dt} \quad (1)$$

where F_X and F_Y represent drag and lift forces respectively with each integral being evaluated around the contour of the cylinder circumference C.

With the aid of the circle theorem [7], the complex velocity potential w, which describes the flow situation pictured in Figure 2, can be written as

$$w = \frac{U(t)c^2}{z} + \frac{i}{2\pi}\sum_{k=1}^{m} , _k \ln(z - z_k) - \frac{i}{2\pi}\sum_{k=1}^{m} , _k \ln\left(z - \frac{c^2}{\bar{z}_k}\right) \quad (2)$$

where $U(t)$ represents the unsteady velocity of the cylinder, c represents the radius of the cylinder, and $, _k$ and z_k represent the strength and position of the kth vortex. This expression is composed of a moving doublet term to model the cylinder, a term to model the m real vortices in the feeding layers and wake, and a term to model the m image vortices in the cylinder. The image vortices are included to ensure that the boundary conditions on the surface of the cylinder are satisfied. Motion of the reference frame fixed at the center of the cylinder is accounted

for by

$$\overline{W} \;=\; U(t) \tag{3}$$

where $\overline{W}$ represents the velocity of the reference frame.

Taking into consideration the expression for the complex potential (Equation 2), the first integral in Equation 1 can be solved using Lagally's theorem [5, 7]

$$i\frac{\rho}{2}\int_C \left(\frac{dw}{dz}\right)^2 dz \;=\; \rho\sum_{k=1}^{m}, _k(-v_k - iu_k) \tag{4}$$

where u_k and v_k are real and imaginary components of the velocity of the center of the kth real vortex.

By integrating by parts [8], and taking advantage of the residue theorem, the second integral of Equation 1 can be written as

$$i\rho\frac{\partial}{\partial t}\int_C \overline{w}\, d\bar{z} \;=\; \rho\sum_{k=1}^{m}\frac{\partial, _k}{\partial t}(q_{k_i} + ip_{k_i}) \;+\; \rho\sum_{k=1}^{m}, _k(v_{k_i} + iu_{k_i}) \;-\; 2\pi\rho c^2\frac{dU}{dt} \tag{5}$$

where p_{k_i} and q_{k_i} are the real and imaginary coordinates of the kth image vortex position and u_{k_i} and v_{k_i} are real and imaginary components of the velocity of the kth image vortex.

By combining Equations 1, 3, 4, and 5 and factoring out the real part, the following expression for the in-line force, F_X, results:

$$F_X \;=\; -\rho\sum_{k=1}^{m}, _k(v_k - v_{k_i}) \;+\; \rho\sum_{k=1}^{m} q_{k_i}\frac{\partial, _k}{\partial t} \;-\; \frac{\pi}{4}\rho D^2\frac{dU}{dt}. \tag{6}$$

Based on an understanding of how vortices in the wake affect the in-line forces, Equation 6 makes sense physically. The first two terms account for the effect of vortices in the feeding layer and the wake. When the vortices are small, their contributions to the drag are small. As the vortices grow, their contribution to the total in-line force increases. The third term is an "added-mass" term, which is a function of the acceleration of the cylinder.

For constant acceleration motion of the cylinder, dimensional analysis shows that

$$\frac{, _k}{UD}, \frac{u_k}{U}, \frac{v_k}{U}, \frac{u_{ki}}{U}, \frac{v_{ki}}{U}, \frac{p_k}{D}, \frac{q_k}{D}, \frac{p_{ki}}{D}, \frac{q_{ki}}{D}$$

are functions of $\frac{s}{D}$ and Re, where s is a measure of how far the cylinder has traveled, D is the cylinder diameter, Re is Reynolds number, and p_k and q_k are position coordinates of the kth real vortex.

Sarpkaya and Garrison [6] showed empirically, with experiments over a broad range of Reynolds numbers ($100 < Re < 5 \times 10^5$),[1] that

$$\frac{, _k}{UD}, \frac{u_k}{U}, \frac{v_k}{U}, \frac{u_{ki}}{U}, \frac{v_{ki}}{U}, \frac{p_k}{D}, \frac{q_k}{D}, \frac{p_{ki}}{D}, \frac{q_{ki}}{D}$$

are functions of $\frac{s}{D}$ *only*. Taking this into consideration, Equation 6 can be reduced to the following:

$$F_X \;=\; -C_m(s/D)\cdot\frac{\pi}{4}\rho D^2\frac{dU}{dt} \;-\; C_d(s/D)\cdot\frac{1}{2}\rho DU^2 \tag{7}$$

where

$$C_m(s/D) \;=\; 1 - \sum_{k=1}^{m}\frac{4}{\pi}\frac{q_{k_i}}{D}\frac{, _k}{UD} \tag{8}$$

$$C_d(s/D) \;=\; 2\sum_{k=1}^{m}\frac{, _k}{UD}\left(\frac{v_k}{U} - \frac{v_{k_i}}{U}\right) \;-\; 2\sum_{k=1}^{m}\frac{q_{k_i}}{D}\frac{\partial(, _k/UD)}{\partial(s/D)}. \tag{9}$$

The key outcome of this 2-D analysis is that for a cylinder undergoing *constant acceleration motions* (relative to nominally still water), the hydrodynamic drag and added-mass coefficients, C_d and C_m, are functions of how far the cylinder has traveled *only*. In other words, the instantaneous values of C_d and C_m are independent of the cylinder's acceleration, its velocity, or the associated Reynolds number and are dependent only on the cylinder's displacement from its initial position at rest.

Strip-Theory Extension to 3-D Using a standard strip-theory approach, the theoretical results of the 2-D analysis can be extended semi-empirically to three dimensions. This approach is diagrammed in Figure 3. The forces acting on a thin segment of the arm are calculated using a form of Equation 7:

$$dF_i \;=\; -C_{m_i}(s_i/D)\cdot\rho\frac{\pi D^2}{4}l_i dl_i\ddot{\theta} \;-\; C_{d_i}(s_i/D)\cdot\frac{1}{2}\rho D l_i^2 dl_i|\dot{\theta}|\dot{\theta}. \tag{10}$$

The hydrodynamic in-line torque and force acting at the hub can be calculated using the following simple relations.

$$dT_i = l_i dF_i \tag{11}$$

$$T_{hyd} = \sum_{i=1}^{n} dT_i \tag{12}$$

$$F_{hyd} = \sum_{i=1}^{n} dF_i \tag{13}$$

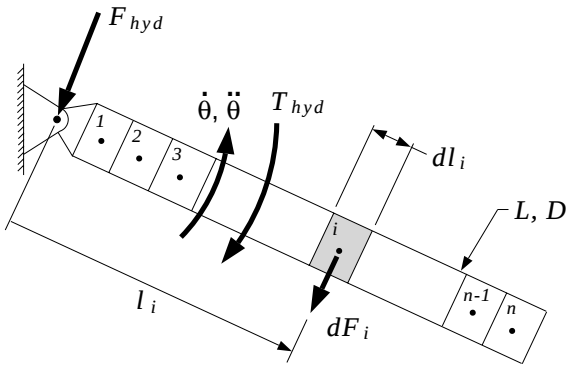

Figure 3: Diagram of Strip-Theory Implementation

where n is the number of segments used in the model.

The conditions under which strip theory can be applied using standard values for coefficients are outlined by Sarpkaya and Isaacson [9]. Flow-visualization experiments have shown that the flow around a swinging circular cylinder is highly three-dimensional [10]. The assumptions under which standard values for the hydrodynamic coefficients (determined under two-dimensional flow conditions) can be used are violated for typical robotic motions due to span-wise flow and end effects. When 3-D flow is significant, model implementations based on strip theory must correct for this through experimental identification of appropriate coefficient values.

3.2 Model Synthesis

Given the relationships of Equations 10 through 12 and measurements of local forces, hub torque, and angular position, velocity, and acceleration of the single-link arm, the challenge remains to determine how the hydrodynamic coefficients, C_d and C_m, vary with respect to the travel or displacement (s/D) of the cylinder. Measurements of torque at the hub of the cylinder are used to determine the effective drag and added-mass coefficients for the entire length of the cylinder. By combining Equations 10 through 12, and assuming that the effects of the local drag and added-mass coefficients can be modeled accurately by global average coefficients $\bar{C}_d$ and $\bar{C}_m$, the following relationship can be written:

$$T_{hyd} = -\sum_{i=1}^{n} \bar{C}_m(s_i/D) \cdot \rho \frac{\pi D^2}{4} l_i^2 dl_i \ddot{\theta} + \bar{C}_d(s_i/D) \cdot \frac{1}{2} \rho D l_i^3 dl_i |\dot{\theta}| \dot{\theta}. \quad (14)$$

[1] For the high-speed arm motions presented here, the value of the peak Reynolds number at the tip of the arm was typically less than 1.5×10^5

Measurements of torque and angular position, velocity, and acceleration were used with Equation 14 to determine $\bar{C}_d$ and $\bar{C}_m$.

Hydrodynamic Coefficient Identification Equation 14 expresses the relationship between the hydrodynamic torque acting and the angular displacement, velocity, and acceleration of the arm — all measured quantities in this research. The unknown parameters of interest are the hydrodynamic drag and added-mass coefficients. The primary challenge in characterizing these coefficients is that for a particular instant in time, Equation 14 is underdetermined. There are two unknown quantities ($\bar{C}_d$ and $\bar{C}_m$) with only one expression to relate them.

To overcome the difficulties in simultaneously identifying values for $\bar{C}_d$ and $\bar{C}_m$, a new approach was developed as part of this research. This approach models $\bar{C}_d$ and $\bar{C}_m$ as a series of cubic-spline polynomials that are functions of s/D. The locations of the spline points, and hence the shape of the polynomial functions modeling the hydrodynamic coefficients, are determined using nonlinear optimization.

Figure 4 illustrates the polynomial spline models used for the drag and added-mass coefficients prior to fitting to the experimental data. Each curve is composed of three types of spline points: one *fixed* point, five *shaping* points, and one *scaling* point. For both coefficients, the fixed points correspond to the start-of-motion values of the coefficients predicted by potential-flow theory: In the initial instants of motion, the value of C_d is fixed at 0 and the value of C_m is fixed at 1. These two points remain unchanged during the optimization process.

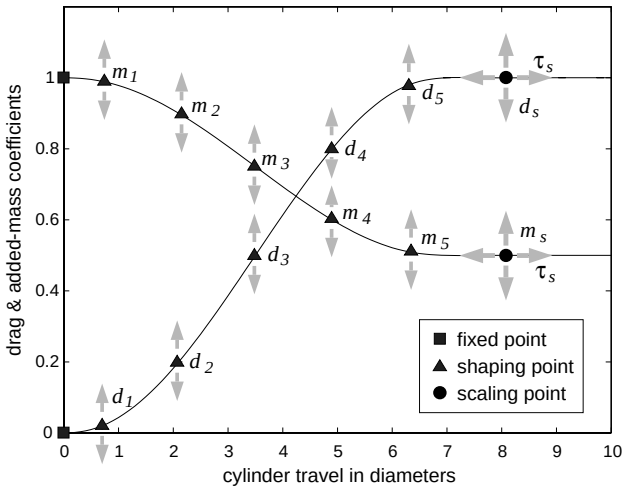

Figure 4: Drag and Added-Mass Coefficient Spline Models

For each coefficient, five equally spaced shaping points are used to vary the shape of the coefficient profile. Movement of these shaping points allows the coefficient curves

to take on a wide variety of shapes that model properly the state-dependent behavior of the coefficients.

Each coefficient curve is scaled both in the travel dimension and the coefficient magnitude dimension by a single scaling point. Movement of this point adjusts the scale of the entire coefficient profile between the fixed point and the scaling point. Location of this scaling point effectively determines the steady-state value of the coefficient and the travel value after which the coefficient is assumed to be constant.

Given measurements of arm position, velocity, acceleration, and hub torque (T_{meas}), the nonlinear optimization problem of fitting the hydrodynamic coefficients to the experimental torque data can be posed as follows:

$$\text{Find } (d_1, d_2, d_3, d_4, d_5, d_s, m_1, m_2, m_3, m_4, m_5, m_s, \tau_s)$$

$$\text{to minimize} \quad \sum_{i=1}^{m} \left(T_{hyd_i} - T_{meas_i}\right)^2 \tag{15}$$

where T_{hyd} comes from Equation 14 and m is the number of data points being considered. For the coefficient data presented below, a total of 12 different arm slews at four different accelerations were used to evaluate the coefficients. For each of the 12 data sets, measurements of hub torque and arm position, velocity, and acceleration at 200 to 500 time points (depending on the duration of the slew) were used to determine the best-fit location of the coefficient spline points. The identification of one coefficient profile for multiple runs of different accelerations is in accordance with the theoretically derived dependence of the coefficients on travel only.

This approach of modeling the coefficients as cubic splines and then using nonlinear optimization to vary the shape of the splines to determine the state-dependent behavior of the coefficients not only enables solution of the problem, but it allows previously determined physical information about the coefficients' behavior to be included in the parameterization of the coefficient profiles.

Experimentally Identified Coefficients Figure 5 shows values for the torque-based drag and added-mass coefficients that were obtained using the optimization procedure described above. Variation of the coefficients for different slews is indicated by the data points marked with '+' symbols. These points were determined by performing the optimization procedure on three groups of data from four different slews (rather than one group of data from 12 slews).

The important thing to note from these results is that they correlate very well with the results from the 2-D theoretical analysis. For $s/D = 0$, the drag and added-mass coefficient values are fixed at 0 and 1 respectively, as potential-flow theory predicts for the case of fully attached

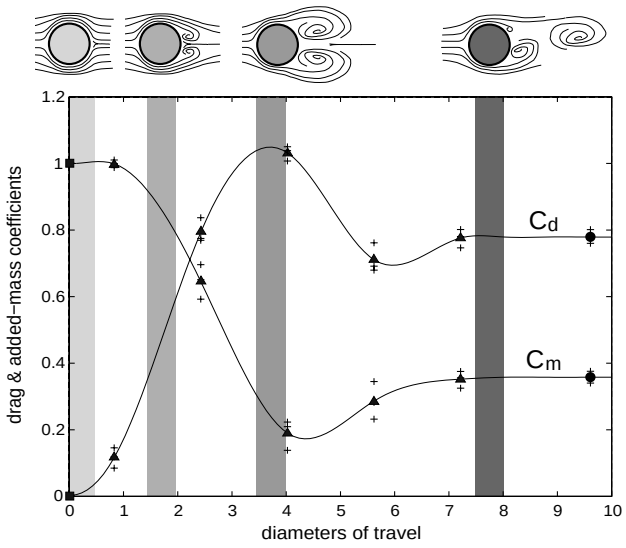

Figure 5: Drag and Added-Mass Coefficients

flow. As the flow separates and a symmetric vortex pair begins to form in the near wake, the drag coefficient rises. The drag coefficient reaches its peak when the vortices are at their largest size just prior to being shed. When the symmetric vortices can no longer coexist in a stable manner in the near wake, vortex shedding begins. When this happens the drag coefficient drops off, after which it rises to its steady-state value corresponding to the fully developed wake.

The dependence of the drag coefficient on the development of vortices in the wake is shown by Equation 9: When no vortices are present, the drag coefficient is zero; as vortices grow and move in the wake, the drag coefficient rises accordingly.

Because of the three-dimensional flows along the span and around the tip, the steady-state drag coefficient (0.78) is considerably lower than the value of 1.2 expected for a translating cylinder with no end effects. Flow around the tip and along the span relieve the low-pressure area at the base (trailing side) of the arm near the tip, resulting in lower drag forces and hence a lower mean drag coefficient.

From the behavior of the added-mass coefficient, it can be concluded that the presence of vortices in the near wake reduces the amount of fluid that is accelerated locally as the cylinder is accelerated. This result is in complete agreement with the results of the two-dimensional potential-flow-theory analysis shown in Equation 8: With no vortices in the wake, $C_m = 1$; as separation occurs and vortices grow in the wake, the added-mass coefficient drops off from this initial value. As long as separation occurs and vorticity is shed into the wake, it is to be expected that the added-mass coefficient will be smaller than the value of 1 predicted by potential-flow theory (without separation effects).

4 Experimental Results

In this section, experimental results validating the accuracy of the model developed in the previous section are given. For the results presented here, the arm was divided into 10 equal segments. This hydrodynamic model is relatively undemanding from a computational point of view and has been implemented at sample rates up to 500 Hz on a 68030-based real-time processor using four segments.

Figures 6 through 8 compare modeled hydrodynamic torque predictions from the model developed here and two other models from the literature with the actual hydrodynamic torques that were measured experimentally. Figure 6 shows results from a short 30-degree, 0.4-second slew, Figure 7 shows results from a 60-degree, 0.6-second slew, while Figure 8 shows results from a longer 120-degree, 1.2-second slew. Results from three different slews are given to demonstrate that the model developed here is valid for a wide range of motions. In each figure, plot (a) shows the time history of the arm motion. Plot (b) shows results from the model developed as part of this research using state-dependent coefficients. Plot (c) shows results from a model implemented according to Lévesque and Richard [2] wherein the effects of added-mass were not considered and the drag coefficient was assumed to a have a constant value of 1.1. Plot (d) shows results from the model inferred from McMillan, *et al.* [3] in which the drag coefficient had a constant value of 1.2 and the added-mass coefficient had a constant value of 1.

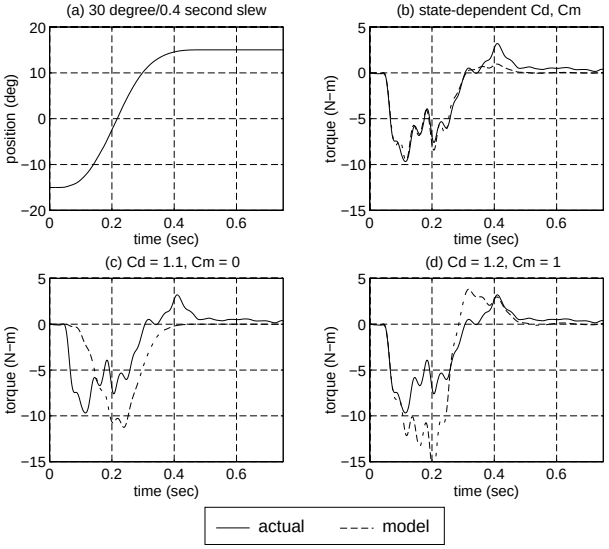

Figure 6: Modeling Results — Short Motion

The results of Figures 6 through 8 demonstrate the improved modeling accuracy of the approach presented here over the most applicable of the other methods presented in the literature. On average, modeling errors were reduced by 4.5 times when comparing the model of this research with the other two models considered.[2] This higher level of accuracy is enabled by the use of *state-dependent* drag and added-mass coefficients. During initial portions of the slews, these coefficients take on values corresponding to values predicted by potential flow theory ($C_d = 0$ and $C_m = 1$). As the motion progresses, the coefficients transition to take on steady-state values corresponding to the three-dimensional separated flow situation ($C_d = 0.78$ and $C_m = 0.36$).

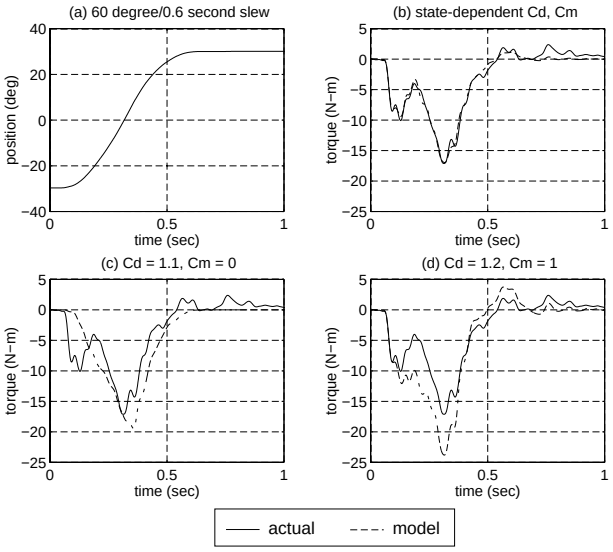

Figure 7: Modeling Results — Medium-length Motion

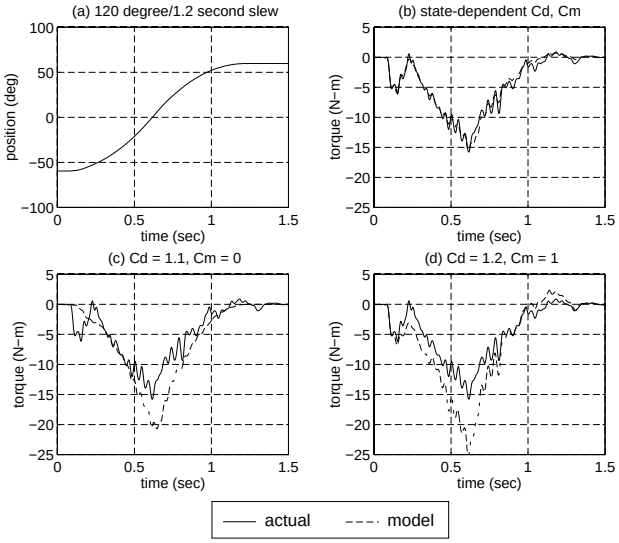

Figure 8: Modeling Results — Long Motion

[2]Model errors were calculated by normalizing the sum of the errors for the data sets presented in Figures 6–8 according to $\sum_{i=1}^{m} |T_{meas_i} - T_{hyd_i}| / \sum_{i=1}^{m} |T_{meas_i}|$, where m is the number of data points.

In plot (c) of Figures 6, 7, and 8 it can be seen that the constant coefficient model fails to capture the effects of the inertial torques, which dominate at the beginning and end of the slew, and that it overestimates the drag during the middle portion of the slew. In the results of plot (d), this constant-coefficient model initially models the inertial torques very well, but later overestimates both the inertial and drag torque components. The major sources of error in the models presented in plots (c) and (d) are due to assuming the coefficients to be constant and assuming that the drag coefficients have the same values as those corresponding to the translational motion of a cylinder (C_d = 1.1–1.2), which they do not because of the radial flow induced by the swinging motion. In other words, the errors can be attributed to using coefficients from a two-dimensional, steady-flow situation to describe a three-dimensional, unsteady flow.

While the data presented in Figures 6, 7 and 8 are for constant-acceleration/constant-deceleration motions, it should be noted that the model developed here has been applied with equal success to fifth-order-spline trajectories, which are common for robotic manipulators.

5 Conclusions

In this paper, the development of an accurate model of the hydrodynamic forces acting on a single-link manipulator has been presented. A two-dimensional potential-flow-theory analysis, which took into account the effects of vortices in the wake, was performed for a cylinder undergoing unsteady motions. The results of this analysis were then extended semi-empirically to three dimensions using strip theory. Measurements of torque were used to gain further physical insight into the hydrodynamic forces acting on the arm and as a basis for the identification of hydrodynamic drag and added-mass coefficients. To enable the identification of these coefficients, an approach based on modeling the state-dependent behavior of the coefficients as cubic-spline functions of arm travel was developed. The net result of these efforts was the implementation and experimental validation of a very accurate hydrodynamic model of the forces acting on swinging single-link arm.

References

[1] Timothy W. McLain, Stephen M. Rock, and Michael J. Lee, "Experiments in the coordination of underwater manipulator and vehicle control", in *Proceedings of Oceans '95 MTS/IEEE*, 1995.

[2] Benoît Lévesque and Marc J. Richard, "Dynamic analysis of a manipulator in a fluid environment", *International Journal of Robotics Research*, vol. 13, no. 3, pp. 221–231, 1994.

[3] Scott McMillan, David E. Orin, and Robert B. McGhee, "Efficient dynamic simulation of an unmanned underwater vehicle with a manipulator", in *Proceedings of the International Conference on Robotics and Automation*, 1994, pp. 1133–1140.

[4] T.J. Tarn, G.A. Shoults, and S. Yang, "Dynamical model for a free-floating underwater robotic vehicle with an n-axis manipulator", in *Proceedings of the U.S.–Portugal Workshop on Undersea Robotics and Intelligent Control*, Lisboa, March 1995.

[5] Turgut Sarpkaya, "Lift, drag, and added-mass coefficients for a circular cylinder immersed in a time-dependent flow", *Journal of Applied Mechanics*, pp. 13–15, March 1963.

[6] Turgut Sarpkaya and C. J. Garrison, "Vortex formation and resistance in unsteady flow", *Journal of Applied Mechanics*, pp. 16–24, March 1963.

[7] L. M. Milne-Thomson, *Theoretical Hydrodynamics*, The MacMillan Company, 4th edition, 1960.

[8] Turgut Sarpkaya, "An analytical study of separated flow about circular cylinders", *ASME Journal of Basic Engineering*, vol. 90, pp. 511–520, 1968.

[9] T. Sarpkaya and M. Isaacson, *Mechanics of Wave Forces on Offshore Structures*, Van Nostrand Reinhold, 1981.

[10] Timothy W. McLain, *Modeling of Underwater Manipulator Hydrodynamics with Application to the Coordinated Control of an Arm/Vehicle System*, PhD thesis, Stanford University, August 1995, Also published as SUDAAR 670.